

## Criticality in the plastic deformation of $L1_2$ intermetallic compounds

D. C. Chrzan and M. J. Mills

*Sandia National Laboratories, Livermore, California 94550*

(Received 5 October 1993; revised manuscript received 22 February 1994)

It is argued that dislocations in the  $L1_2$  intermetallic compounds displaying the yield strength anomaly undergo a stress-driven pinning-depinning transition. The transition is from a dynamic phase in which a moving dislocation becomes immobile to a dynamic phase in which a moving dislocation, in an infinite medium, remains mobile for all time. The distribution of event times and areas, where an "event" is the mobilization and subsequent immobilization of a dislocation, is related to measurements of the primary creep transient. At the critical point of the proposed transition, the distribution of events becomes scale invariant. A simple scaling hypothesis connects the scaling behavior of the transition to the time dependence of the creep tests. A simplified model of dislocation motion is presented and used to study the properties of the transition. The properties so calculated are not obviously consistent with the published *interpretations* of experiments, but are consistent with the published *data*. A reinterpretation of those experiments is proposed.

### I. INTRODUCTION

It is argued below that the dislocations responsible for the plastic deformation in  $L1_2$  compounds undergo a stress-driven pinning-depinning transition. A simple scaling argument is used to connect the continuous nature of this transition to the mechanical properties of the compounds. It is demonstrated that primary-creep-transient measurements provide a means to determine important characteristics of the transition.

This paper is organized as follows. This section is an introduction containing background on the mechanical properties of these intermetallics. In Sec. II a model is presented which establishes the connection between the pinning-depinning transition and the primary-creep transient. Section III introduces the simulations used to study the transition. Section IV contains a numerical study of the transition, including results for the critical exponents. Section V presents a discussion of the experimental results predicted by the theory. Finally, Sec. VI presents the conclusions.

The current understanding of plastic deformation in the  $L1_2$  intermetallics relies on both experimental and theoretical research efforts spanning more than 20 years. A summary of experimental and theoretical results relevant to this paper is presented in the following.

The  $L1_2$  intermetallic compounds are technologically important. Unlike most metals which get weaker with increasing temperature, the strength of many  $L1_2$  compounds *increases* with temperature over a range of temperatures.<sup>1</sup> It is this "anomalous flow" behavior which leads to the use of these compounds in high-temperature structural applications. For example, the primary component of modern superalloys used for turbine blades in jet engines is based on the ordered phase of  $Ni_3Al$ . As the temperature of a typical compound is increased from 300 to 900 K, the yield strength increases, approximately by a factor of 9.<sup>2</sup>

The anomalous temperature dependence of the yield strength is due to the tendency of the dislocations to form nonplanar core structures.<sup>3,4</sup> Since the Burgers vectors of these dislocations are vectors of the superlattice, the dislocations are referred to as superdislocations. Figure 1(a) depicts the presumed core structure of a glissile superdislocation. The superdislocation has a Burgers vector  $a\langle 101 \rangle$ , where  $a$  is the cubic lattice constant. In general, the energy of a dislocation scales with the square of the magnitude of its Burgers vector. It is therefore energetically favorable for the superdislocation to dissociate into two superpartial dislocations, each with Burgers vector  $a/2\langle 101 \rangle$ . The region between the dissociated superpartials now contains a (111) antiphase boundary (APB). The equilibrium separation between superpartials is determined by the balance of the repulsive elastic interaction between the superpartials and the surface tension due to the APB. The superpartial dislocations are thus bound by the APB. Each superpartial dislocation can further lower its energy by dissociation into two  $a/6\langle 112 \rangle$  Shockley partials. The Shockley partials are bound by a region of crystal containing a complex stacking fault (CSF). In this configuration, in which the four Shockley partials of a single superdislocation lie in a single (111) plane, the superdislocation is mobile.

Both microstructural and theoretical evidence suggest that the planar, glissile configuration is not the lowest-energy configuration. Superdislocations have a tendency to "cross slip" from the (111) plane to the (010) plane. The completely cross-slipped configuration, referred to as a Kear-Wiltsdorf lock,<sup>5</sup> is shown in Fig. 1(b). This cross-slip tendency arises from two sources: The (010) APB energy is lower than the (111) APB energy,<sup>6</sup> and the elastic interaction between superpartials generates a torque which also drives the cross slip.<sup>7</sup>

Paidar, Pope, and Vitek<sup>8</sup> (PPV) proposed that cross slip is a thermally activated process leading to the formation of a localized pinning point. This pinning point is shown in Fig. 1(c). Note that PPV have assumed that,

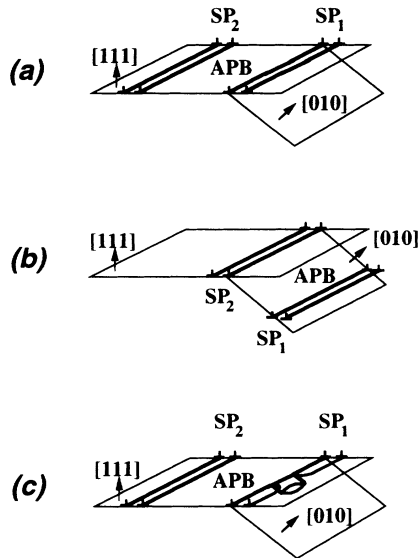


FIG. 1. Three possible core configurations of the screw superdislocations in the  $L_{12}$  intermetallics: (a) the assumed structure of a glissile superdislocation, (b) the cross-slipped state, a Kear-Wilford lock Ref. (5), and (c) the formation of a cross-slip-pinning point.  $SP_1$  refers to the forward superpartial, and  $SP_2$  refers to the rearward superpartial. APB denotes an antiphase boundary. In panels (a) and (c), the antiphase boundary is of the (111) type. The Kear-Wilford lock of panel (b) contains a (010) APB. In all cases, the superpartials are dissociated into two Shockley partials. The Shockley partials are connected by a (111) complex stacking fault. Thermally activated constriction of this stacking fault is required for cross slip to occur.

under an applied stress, complete cross slip [Fig. 1(b)] is dynamically impossible. The superdislocation is envisioned, by PPV, to move as shown in Fig. 2. In the initial state, pinning points have formed at the sites labeled  $A$ . The superdislocation bows around the pinning points, exerting a force on them. Eventually, this force reaches a critical value at a critical bowing angle  $\theta_c$  (the bowing angle is measured between the superdislocation's line direction and the screw orientation). At this point, the bowing force is sufficient to overcome the pinning points, and they dissolve. Simultaneously, however, new pinning

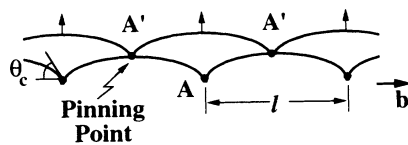


FIG. 2. Illustrations of successive positions for a superdislocation moving on the (111) plane by bowing between the localized pinning points as envisioned by PPV. Note that the pinning points are assumed to form in a regular array. The periodic length between pinning points is indicated as  $l$ . The superdislocation bows between these obstacles, exerting a force on them. When this angle reaches the critical value,  $\theta_c$  in the figure, the obstacles at  $A$  are assumed to dissolve. Concomitantly, new obstacles are assumed to form at  $A'$ . The Burgers vector  $\mathbf{b}$  is indicated.

points are envisioned to form at the points labeled  $A'$ , thus establishing a "steady state." Note that at lower stresses it is possible for the line tension in the superdislocation to prevent bowing to the critical angle. In this configuration, all the segments in the PPV-like superdislocations become immobile—the superdislocation is pinned. As the temperature increases, the frequency of the formation of the pinning points increases, thus reducing the average distance between pinning points. This decreased distance, in turn, requires that a larger stress be applied to allow the segments to bow to the critical angle. This is the microscopic process responsible for the yield strength increase.

There are several details of the cross-slip pinning process which are of importance to what follows. First, the frequency of cross slip increases with temperature. Second, in order for cross slip to occur, the superdislocation must be oriented along the screw direction. Third, a pinning point dissolves (athermally) when the adjacent superdislocation segment bows to a critical bowing angle.

Direct simulation of dislocation motion resulting from the PPV model of an individual pinning point, but *without* the artificially imposed spatial and temporal correlations between pinning events, allows a detailed study of the dynamics of superdislocation motion<sup>9,10</sup> (for brevity, "dislocation" will henceforth refer to the total  $a\langle 101 \rangle$  Burgers vector of the superdislocation). These studies reveal features of the dislocation motion that are relevant to the current work. Most importantly, the dislocation line tension and the physical constraints on the formation of pinning points lead to correlations between the pinning points.

Consider the expansion of an (initially) circular loop. Since only screw-oriented segments can pin, the edge portion of the loops move rapidly, unhindered by cross-slip pinning. The dynamical motion of the screw segments, however, depends on the applied stress. At lower stresses, the dynamics lead to a structure in which pinning points tend to form very near to other pinning points. This results in long segments of near-screw orientation which are highly pinned and, hence, immobile. These highly pinned, immobile segments are connected by long, unpinned, segments of mixed orientation referred to as superkinks. The observed steplike configurations are similar to those observed using transmission electron microscopy.<sup>9,11</sup> In the studies reported in Refs. 9 and 10, the near-screw dislocations are found to advance forward (i.e., in the direction orthogonal to the Burgers vector indicated in the figure) through the *lateral* motion of superkinks. Therefore superkink motion governs glide in these compounds.

At high stresses, the loops appear substantially different from their low-stress counterparts. The pinning points are more uniformly spaced, and the screw segments of the dislocation move nearly as rapidly as the edge segments. In addition, the long, mixed-character superkinks which appear at lower stresses are absent. (See Ref. 9 for details.)

In a finite-size crystal, the edge segments of the dislocation loops rapidly advance out of the crystal, leaving the predominantly screw segments. The mechanical proper-

ties of the compound, then, depend on the mobility of these predominantly screw-oriented dislocations. At low stresses, these segments are observed to advance for some time and then become immobile. As detailed previously,<sup>9,10,12</sup> this immobilization occurs because the number of mobile superkinks in a dislocation fluctuates with time as a result of superkink multiplication, annihilation, and interaction. Eventually, these fluctuations lead to a configuration in which there are no mobile superkinks within the dislocation. This immobilization of dislocations, referred to below as exhaustion, is a natural explanation of the strain hardening in the compounds. In contrast, at high stresses, the predominantly screw-oriented segments move at a nearly constant velocity for as long as they can be observed (limited by computer time).

The above characterization is indicative of a change in the correlations between the pinning events. At low stresses, these correlations result in total pinning of the entire dislocation, whereas at high stresses the localized pinning events are only capable of retarding dislocation motion. Thus the dislocations display a stress-driven pinning-depinning transition, and it is this transition which is studied below. It is important that the pinning-depinning transition not be confused with the localized pinning event. The pinning-depinning transition involves the pinning of the *entire* dislocation, a collective effect arising from the correlations between localized pinning points. It is also noteworthy that, within the physical picture presented in Refs. 9, 10, and 12, the mechanical properties of the compounds, while linked to the properties of the localized pinning points, are not determined solely by those properties. Rather, it is the collective behavior of the localized pinning points which leads to the observed dislocation dynamics. *Thus, in bridging the length-scale "gap" between atomistics and macroscopic mechanical properties, one is forced to consider collective effects.*<sup>10</sup>

The results of creep tests are of particular interest to this paper. A creep test measures the strain as function of time for a sample subject to a constant stress. The early-time portion of this curve is referred to as the primary-creep transient.

Thornton, Davies, and Johnston<sup>1</sup> (TDJ) measured creep in polycrystalline samples of Ni<sub>3</sub>Al. They found that at lower temperatures (298 K) the strain rate continually decreased as a function of time and the reported form of the transient was well described, for a range of times, by

$$\epsilon(t) \sim \ln t, \quad (1)$$

where  $\epsilon(t)$  is the tensile strain at time  $t$ . At higher temperatures (672 K), they found that for low stresses the primary-creep transient was again logarithmic in time. However, at higher stresses, the primary-creep transient became proportional to  $t^{1/3}$ :

$$\epsilon(t) \sim t^{1/3}. \quad (2)$$

It is important to note that the time dependences of Eqs. (1) and (2) are *assumed*—no detailed theory of dislocation motion in the  $L1_2$  compounds has been proposed

to support them. (Historically, logarithmic creep is assumed to arise from dislocation mobility controlled creep, whereas  $t^{1/3}$  creep is assumed to stem from recovery processes.) It is also noted that based on the figures in TDJ's work<sup>1</sup> these forms apply only over a limited time range. *Thus, although TDJ assumed a simple power-law dependence for the creep transient, the experiments reveal clearly a more complicated time dependence.*

## II. CRITICALITY AND MECHANICAL PROPERTIES

Simulations demonstrate that the movement of dislocations (at low stresses) in the compounds under consideration is accomplished through the lateral motion of superkinks.<sup>9</sup> As a dislocation advances under an applied stress, its superkink population distribution fluctuates. Consequently, the time and area swept out before exhaustion also varies (from dislocation to dislocation). Characterization of this distribution of times and areas provides a description of transient plastic flow.

Consider a crystal with a large number of noninteracting dislocations. (The dislocations in the  $L1_2$  compounds are not observed to be directly entangled. Under these circumstances, the dislocations interact only through their elastic stress fields. This interaction, admittedly important, is neglected in the current work and the need for further research is noted.) Imagine that the crystal has been strained so that the vast majority of the dislocations are the linear, mostly screw-character dislocations described in the preceding section. Also, assume that a stress is applied until the sample no longer creeps (i.e., all of the dislocations are exhausted). The stress is then incremented and held fixed. Some dislocations now become mobile, because the increased stress is sufficient to bow some formerly immobile segments beyond the critical angle.

Let  $n(a, t) da dt$  be the number of dislocations which subsequently sweep out an area between  $a$  and  $a + da$  before exhausting at a time between  $t$  and  $t + dt$ . The total number of dislocations which exhaust between time  $t$  and  $t + dt$  is  $\bar{n}(t) dt$  with  $\bar{n}(t)$  given by

$$\bar{n}(t) = \int_0^\infty da n(a, t). \quad (3)$$

Similarly,  $\bar{n}(a) da$  is the total number of dislocations which sweep out an area between  $a$  and  $a + da$  with  $\bar{n}(a)$  given by

$$\bar{n}(a) = \int_0^\infty dt n(a, t). \quad (4)$$

The average area swept out by a dislocation which moves for a time between  $t$  and  $t + dt$  before exhausting is given by

$$\bar{a}(t) = \frac{\int_0^\infty da a n(a, t)}{\int_0^\infty da n(a, t)}. \quad (5)$$

Let  $v(t, t')$  be the average areal velocity, at time  $t$ , of a dislocation destined to exhaust at time  $t'$ . The definition of  $v(t, t')$  requires that

$$v(t, t') = 0, \quad \forall t \geq t'. \quad (6)$$

Also, from the definition of  $v(t, t')$ ,

$$\bar{a}(t) = \int_0^t dt' v(t', t). \quad (7)$$

The shear strain  $\gamma(t)$  is proportional to the total area swept out by all the dislocations. The experimentally measured shear-strain rate  $d\gamma(t)/dt$  is proportional to  $dA(t)/dt$ ,

$$\frac{dA(t)}{dt} = \int_t^\infty dt' v(t, t') \bar{n}(t'). \quad (8)$$

This expression follows directly from the definition of  $\bar{n}(t)dt$  and  $v(t, t')$ . Thus the time-dependent flow properties of the material are related directly to the exhaustion distribution.

Pinning-depinning transitions in charge-density waves have been described within the framework used for continuous phase transitions.<sup>13</sup> A notable feature of continuous phase transitions is that they display scale invariance at a critical point. By analogy, it is proposed that the critical point of the pinning-depinning transition studied here displays scale invariance at a critical stress. Physically, the critical stress is the result of the competition between the thermally assisted formation of pinning points and their dynamically driven annihilation. At low stresses, the formation rate is larger than the annihilation rate, leading to pinning of the entire dislocation. At stresses above the critical stress, the pinning-point annihilation rate equals the formation rate, and on the average, the density of pinning points remains constant while the dislocation remains mobile. Because the pinning-point formation rate is temperature dependent, the critical stress is also temperature dependent.

In order to explore the consequences of the proposed scale invariance, it is conjectured that at a critical stress the exhaustion distribution  $n(a, t)$  displays scale invariance:

$$\lambda n(a, t) = n(\lambda^\alpha a, \lambda^\delta t), \quad (9)$$

where  $\alpha$  and  $\delta$  are the scaling exponents.

The scaling ansatz (9) implies that quantities related to the exhaustion distribution will obey simple power-law relationships (at the critical point) with exponents directly related to  $\alpha$  and  $\delta$ . For example,

$$\bar{n}(t) \sim t^{-\xi}, \quad \xi = -(1 + \alpha)/\delta. \quad (10)$$

Similarly,

$$\bar{n}(a) \sim a^{-\beta}, \quad \beta = -(1 + \delta)/\alpha. \quad (11)$$

More relevant to primary creep,

$$\frac{dA(t)}{dt} \sim t^{-\Delta}, \quad \Delta = -(1 + 2\alpha)/\delta. \quad (12)$$

A power-law creep rate is the direct result of the scale invariance of the exhaustion distribution—in an infinite system, at the critical stress.

There is, however, another observation that needs consideration. The TDJ analysis resulted in a range of stresses for which a logarithmic primary-creep transient was observed (over a range of times), not just a single critical stress. In addition, TDJ reported a range of stresses

for which the primary-creep transient varied as  $t^{1/3}$  (again, over a limited time span). A complete theory of primary creep in the  $L1_2$  alloys must be able to predict the algebraic laws over a broad range of stresses in order to be compatible with the experiments.

In order to explain a power-law creep rate over a range of stresses, one is forced to consider the behavior of the dislocations near, but not at, the critical stress. In many systems displaying scale invariance at a critical point, it is observed that the function which becomes scale invariant at the critical point is well described by the Ornstein-Zernike<sup>14</sup> form near the critical point. The following is, therefore, conjectured to hold near to and below the critical stress:

$$\bar{n}(t) = \bar{n}_t t^{-\xi} e^{-t/t_0}, \quad (13)$$

where  $t_0$  is the characteristic exhaustion time of the dislocation, which becomes infinite at the critical point, and  $\bar{n}_t$  is a normalization constant. The value of  $\bar{n}_t$  is determined by requiring that the integral of  $\bar{n}(t)$  from some initial time (nonzero) to infinite times be equal to the number of mobile dislocations at that initial time. Note that no analytical theory has been developed to support the form of Eq. (13). However, this form produces a high-quality fit to the numerically obtained distributions.

The velocity function  $v(t, t')$  is the function which describes the average, time-dependent velocity of a dislocation destined to exhaust at time  $t'$ . Scale invariance implies that there is no characteristic exhaustion time in the distribution  $\bar{n}(t)dt$  [i.e.,  $t_0 \rightarrow \infty$  in Eq. (13)]. Consider a dislocation destined to exhaust at time  $t'$ . This time provides a characteristic time for that particular exhaustion event. Since there is no other characteristic time in the dynamics, one must be able to write the following (at the critical point in an infinite system):

$$v(t, t') = t'^\eta g(t/t'), \quad (14)$$

where  $\eta$  is a scaling exponent and  $g(x)$  is defined to be the areal-velocity scaling function. Using Eqs. (5) and (7), one can show that  $\eta$  is related to  $\alpha$  and  $\delta$ :

$$\eta = \alpha/\delta - 1. \quad (15)$$

Using expressions (13) and (14) with expression (8) gives the following equation for the creep strain rate at stresses near the critical stress:

$$\frac{d\gamma(t)}{dt} = \frac{\bar{n}_t b}{V} t^{1+\eta-\xi} \int_0^1 \frac{dx g(x) \exp(-x/t_0)}{x^{2+\eta-\xi}}, \quad (16)$$

where  $b$  is the magnitude of the Burgers vector,  $V$  is volume of the crystal, and it has been assumed that Eq. (14) holds near the critical stress. (This is certainly a good approximation for  $t' \ll t_0$ .) Thus, at the critical stress, when  $t_0$  is strictly infinite, the creep rate reduces to the simple power law of Eq. (12) with  $\Delta = \xi - \eta - 1$ . (In the case  $\Delta = 0$ , the preceding statement does not hold.)

It is difficult to extract the behavior of  $d\gamma(t)/dt$  for  $t_0$  large, but finite, without knowledge of the critical exponents and the areal-velocity scaling function. However, if one assumes that  $g(x)$  can be written as a polynomi-

al in  $x$  (i.e.,  $g(x)$  can be expanded in a complete set of polynomials defined on the interval  $[0,1]$ ),

$$g(x) = \sum_{m=0}^{\infty} g_m x^m, \quad (17)$$

then Eq. (16) can be recast:

$$\frac{d\gamma(t)}{dt} = \frac{\bar{n}_i b}{V} t^{1+\eta-\xi} \sum_{m=0}^{\infty} g_m \int_1^{\infty} \frac{dx \exp(-xt/t_0)}{x^{m+\xi-\eta}}. \quad (18)$$

In summary, the distribution of dislocation exhaustion events,  $n(a,t)da dt$ , is linked to the mechanical properties of the  $L1_2$  compounds. The continuous nature of the proposed pinning-depinning transition leads directly to the algebraic form for the primary-creep transient. Quantitative evidence supporting this claim, however, has not been given. Therefore, in the following sections, a model for dislocation motion is introduced and studied. The model displays the proposed transition and allows a detailed study of its properties.

### III. SIMPLIFIED DISLOCATION MODEL

Continuum-based simulations<sup>9</sup> are too numerically intensive to allow direct calculation of the properties of the proposed transition. Therefore a simplified model of dislocation motion is developed. The study of this model provides a useful qualitative information concerning the nature of the transition, as well as quantitative estimates of the scaling exponents.

A remarkable feature of critical exponents for equilibrium phase transitions is their universality.<sup>15</sup> If one constructs a model with the proper symmetry, it is possible to determine the critical exponents very accurately. While universality has not been explicitly shown to hold for nonequilibrium systems, it is possible that the exponents for nonequilibrium phenomena display behavior dependent only on symmetries, not precise microscopic details. This possibility has been exploited in studies of crystal growth.<sup>16</sup> In addition, recent results on a simplified Burridge-Knopoff model have demonstrated universality for that particular dynamical system.<sup>17</sup> In the problem under consideration here, it is not clear what symmetries determine the exponents. Therefore the approach taken is to develop a model which mimics the physics of the dislocations as closely as possible while maintaining computational tractability. It is hoped that the model studied here can make quantitative predictions for the pinning-depinning transition.

In constructing a model for dislocation motion, it is necessary to preserve the physical properties of a superkink. In particular, it is essential to represent properly the superkink-superkink interactions as well as the interaction of the superkinks with the pinned dislocation structure (i.e., the "backbone" of the dislocation). The model presented here includes the processes thought to be important to the description of dislocation motion: (1) Superkinks spawn superkinks, (2) superkinks can annihilate through interactions with the "backbone," and (3) superkink-superkink interactions can lead to the destruc-

tion of one or more superkinks. The rules governing the model are described in general terms immediately below. In order to make the dynamics stemming from the rules more clear, specific examples of superkink motion within the model are also presented.

The simplification begins by describing the dislocation in a manner similar to that encountered in crystal-growth models.<sup>16</sup> The dislocation is assumed to consist of  $L$  segments, labeled by the index  $i$ . Each segment  $i$  rests at a position given by  $y_i$ , restricted to be an integer. For each step of the model, the segment at each point  $i$  is allowed to advance with an advancement probability  $p_i$  that depends on the configuration of that segment's nearest neighbors.  $L$  random numbers  $p_{i0}$ , uniformly distributed between 0 and 1, are generated. The advancement of the dislocation is accomplished through the rule

$$y_i = \begin{cases} y_i + 1, & p_i > p_{i0}, \\ y_i, & p_i \leq p_{i0}. \end{cases} \quad (19)$$

The physics of the model is contained in the specification of the advancement probabilities.

Figure 3 depicts the possible configurations of nearest-neighbor sites which are allowed in the model. In this model, a mobile superkink is composed of one segment drawn from configurations (l)–(o), any number of segments of type (g), and one segment drawn from (h)–(k). Figure 4 shows the model representation of one type of superkink (there are numerous possible configurations displaying superkink behavior). For the purposes of this discussion, a configuration of sites will be denoted

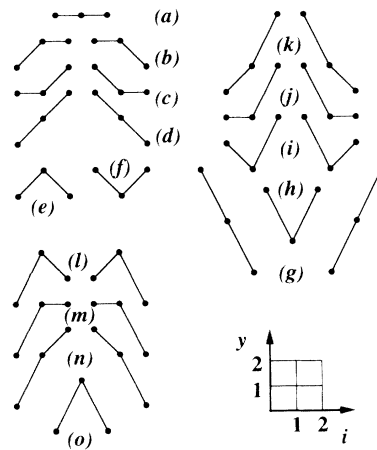


FIG. 3. Three segment configurations allowed by the model. The darkened points represent segments, not pinning points. In this model, a superkink is composed of one segment drawn from configurations (l)–(o), any number of segments (g), and a segment drawn from configurations (h)–(k). Segments labeled (a)–(f) are assumed to be immobile because they do not have sufficient edge character. Segments (g) are mobile because they have sufficient edge character. Segments (h)–(k) are mobile because they represent the bottom portion of the superkink which is freeing the adjacent pinning point. Configurations (l)–(o) are partially mobile because they represent the upper edge of a superkink. See the text for more details. The lower right corner of the figure is the scale.

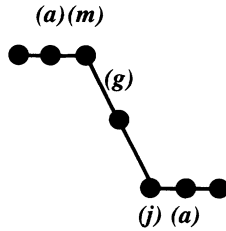


FIG. 4. Example of a superkink. The segment types (see Fig. 3) composing the superkink are indicated. A configuration of segments is denoted through a sequence of letters. In this case, the superkink is denoted [(a)(m)(g)(j)(a)]. See the text for details.

through a succession of letters. For example, the superkink shown in Fig. 4 is indicated by [(a)(m)(g)(j)(a)] because it contains one segment in which the sites have a nearest-neighbor arrangement of type (a), adjacent to a segment of type (m), etc. The advancement of the dislocation in the screw direction is accomplished through the lateral motion of unpinned segments with a sufficient degree of edge character.<sup>9</sup> For the purposes of this simple model, the edge character of a segment is determined by the position of the neighboring sites. If both  $|y_{i-1} - y_i|$  and  $|y_{i+1} - y_i|$  are less than 2, site  $i$  is deemed to have insufficient edge character for mobility and is immobile. The central sites in the configurations labeled (a)–(f) are, therefore, immobile and have  $p_i = 0$ . The central sites in the configurations labeled (g) are defined to be mobile,  $p_i = 1$ , because they represent the maximum edge character of any segment in the model. In the continuum simulations, a pinning point dissolves when the dissolution force reaches a critical value. In this discrete model, the dissolution force exerted on site  $i$  is critical whenever  $(y_{i-1} - y_i)$  and/or  $(y_{i+1} - y_i)$  are equal to 2. Configurations labeled (h)–(k), therefore, have  $p_i = 1$ . The central sites in (l)–(o) are those which are potentially mobile. Their advancement probabilities depend on the temperature and the applied stress in the manner outlined below.

Configurations (l)–(o) correspond to regions of the dislocations in which new pinning points can form. In order to determine the advancement probabilities for the four configurations (l)–(o), one must account for how the equivalent points would move in the continuum model. The illustration of Fig. 5 demonstrates the origin of the correlations between pinning points. The shaded region, the “pinning zone,” is the region near a pinning point in which another pinning point can form and create an immobile segment.<sup>9</sup> The shape of this region is dictated by the critical bowing angle  $\theta_c$  and the applied stress. The total probability for pinning of an adjacent point is roughly proportional to the time that the dislocation segment spends in the “pinning zone.” To a first approximation, the time spent in this pinning zone is inversely proportional to the velocity of the dislocation segment. The velocity of the segment is directly proportional to the difference of the applied stress and the bowing stress, with the bowing stress proportional to the circular curvature  $\kappa_i$  of the segment. Therefore the probability that a segment  $i$  pins is given by

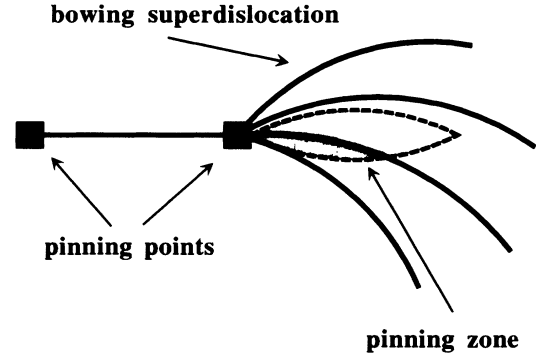


FIG. 5. Origins of the correlations between pinning events. There is only a small region near which a pinning point can form and create an immobile segment, indicated by the shaded area, the “pinning zone.” At low stresses, the dislocation spends an appreciable time in this “pinning zone,” and there is a high probability of pinning. Increasing stress has two important effects. First, the size of the shaded region decreases. Second, the dislocation moves more rapidly. Both of these effects reduce the probability of forming an immobile segment (Ref. 9).

$$p_{\text{pin}}(i) \sim \frac{\Theta}{\tau - \kappa_i}, \quad (20)$$

where  $\tau$  is a parameter representing the applied stress and  $\Theta$  is a parameter reflecting the pinning frequency. Since the pinning frequency increases with temperature,  $\Theta$  also increases with temperature. The advancement probabilities for configurations (l)–(o) are then given by

$$p_i = \max \left\{ 0, 1 - \frac{\Theta}{\tau - \kappa_i} \right\}, \quad (21)$$

where

$$\kappa_i = \frac{\partial^2 y}{\partial x^2}(i) \left[ 1 + \left[ \frac{\partial y}{\partial x}(i) \right]^2 \right]^{-3/2} \quad (22)$$

and the derivatives are replaced by their discrete counterparts:

$$\frac{\partial y}{\partial x}(i) \approx \frac{[y_{i+1} - y_{i-1}]}{2} \quad (23)$$

and

$$\frac{\partial^2 y}{\partial x^2}(i) \approx [y_{i+1} + y_{i-1} - 2y_i]. \quad (24)$$

The advancement probabilities are thus determined by two parameters  $\Theta$  and  $\tau$ .

The dynamics of superkink motion are most easily explored through example. Consider the superkink of type [(a)(m)(g)(j)(a)] shown at the far left of Fig. 6. The figure displays three of the possible paths for the superkink. The path labeled by the arrow (A) takes the configuration [(a)(m)(g)(j)(a)] to the configuration [(a)(b)(n)(k)(c)]. The path labeled by the arrows (A) and (C) is the path by which the superkink moves laterally one unit (in two time steps) and returns to its initial configuration. If  $P(z)$

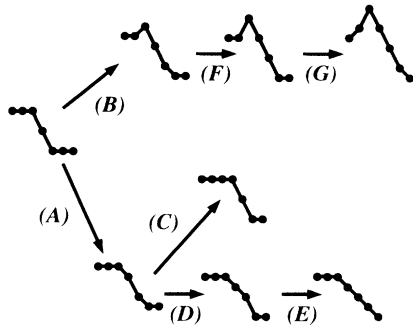


FIG. 6. Example of superkink motion demonstrating three typical behaviors. The path designated by the arrows (A) and (C) returns the superkink to its original structure, but translates the superkink by one lateral spacing. The path (A)–(D)–(E) leads to immobilization of the superkink. The path (B)–(F)–(G) leads to spawning of an additional superkink.

denotes the advancement probability of a configuration of type  $(z)$  [where  $(z)$  is any configuration (a)–(o) of Fig. 3], then the probability that configuration [(a)(m)(g)(j)(a)] will return to itself (translated laterally by one space) in two time steps is given by the product

$$[1 - P(m)]P(n). \quad (25)$$

The term in square brackets represents the probability that the original configuration will take the path labeled (A) in the figure, and the second term represents the probability that the subsequent configuration will be that resulting from path (C). Alternatively, the mobile superkink could have taken path (A)–(D)–(E), which would result in annihilation of the mobile superkink. The probability for the superkink to annihilate through this path (there are *many* paths to annihilation) is given by

$$[1 - P(m)][1 - P(n)]^2. \quad (26)$$

Had the original superkink evolved along the path (B)–(F)–(G), another mobile superkink would have been spawned. The probability of this path can be calculated as well. Note that the spawned mobile superkink moves in a direction opposite to that of the original superkink. In addition to superkink motion, annihilation, and spawning, the interaction of one superkink with another is also allowed in the model. Thus the primary processes identified from the continuum simulations are incorporated in this discrete model.

Transition probabilities similar to those of Eqs. (25) and (26) can be written down for all possible configurations of  $L$  segments. In principle, the distribution  $n(a, t) da dt$  can be calculated exactly from these probabilities. In practice, however, the number of possible configurations grows as  $5^{(L-1)}$ , and the transfer matrix connecting the various configurations becomes intractable for moderate  $L$ . The exact solution for  $L=4$  has been obtained through this technique, and it agrees with the simulated results for the model for a system of this size. However, the scaling behavior manifests itself through the large number of degrees of freedom found only in systems of large  $L$ . This fact emphasizes the col-

lective nature of the transition. It is thus necessary to use numerical methods to explore the properties of the model described above.

The dynamics of the model are explored as follows. A random, immobile configuration of the dislocation is generated using the configurations of Fig. 3 labeled (a)–(f). A dislocation is mobilized by selecting a point at random in the dislocation and allowing it to advance by one unit. The dislocation advances according to the rule (19) with the advancement probabilities described above until it becomes completely immobile. Throughout the simulation the dislocation is restricted to approach the boundaries of the crystal with zero slope—the end segments (those labeled  $i=1$  and  $i=L$ ) are drawn always from one of the configurations (a), (e), (f), (h), and (o). A dislocation becomes immobile when all of its segments are drawn from the configurations (a)–(f). The total area swept out by the dislocation and the time span over which the dislocation is mobile are noted. Starting from the exhausted configuration, the dislocation is remobilized by advancement of a random point. In this manner, the distribution of exhaustion events,  $n(a, t) da dt$ , predicted by the model is numerically calculated.

#### IV. RESULTS FROM NUMERICAL STUDY OF THE MODEL

As stated above, it is hoped that the model can make quantitative predictions for the critical exponents. The model is also useful for analyzing qualitative aspects of dislocation motion, and these aspects are discussed in Sec. IV A below. Section IV B contains a study of the scaling properties of the transition, including a brief discussion of the effects of finite size.

##### A. General features of dislocation motion

Figure 7(a) depicts the exhausted configurations of a single dislocation advancing according to the rules described in the preceding section. For this simulation, the length of the dislocation was chosen to be  $L=100$ , with the temperature parameter  $\Theta=6.5$  and the stress parameter  $\tau=10.0$ . At this stress, the dislocation is mobile typically for only a short time before exhaustion and consequently sweeps out small areas (the area swept out by an event is the white region in the plots). This behavior is consistent with the exponential cutoff in Eq. (13). Figure 7(b) plots the exhausted configurations of a dislocation with  $\Theta=6.5$  and  $\tau=12.0$ . At this stress, the number of larger events is substantial, but there appears to be an even larger number of small events. (The “size” of an event can be gauged by the area it sweeps out.) In this regime, the dislocation advances by the lateral motion of inclined segments (with slopes equal to 2), while the majority of the dislocation remains static. This behavior is in qualitative agreement with the superkinklike motion of dislocations found in the continuum-based model<sup>9</sup> and indicates that the dynamics of the current model are reasonable. Figure 7(c) shows the exhausted configurations of a dislocation advancing under an applied stress of  $\tau=15.0$  with  $\Theta=6.5$ . As is evident from

the figure, the distribution of events sizes is dominated by very large (both in area and time) events. These large events involve the motion of the entire dislocation and may be described by collective dynamics differing from those of the smaller-scale events. It has been argued in the context of charge-density-wave systems that the critical behavior of a finite-size system is distinctly different from that of an infinite system.<sup>13</sup> Perhaps the difference in dynamics of the larger and smaller events of the present model is related to a similar difference.

The nature of the stress-driven pinning-depinning transition is now clear. Below the critical stress, the “events” (i.e., the mobilization and subsequent immobilization of a dislocation) are limited by some time intrinsic to the dynamics of dislocation motion. As the stress increases, this intrinsic time also increases. Consequently, the distribution of the “sizes” of the “events” begins to display

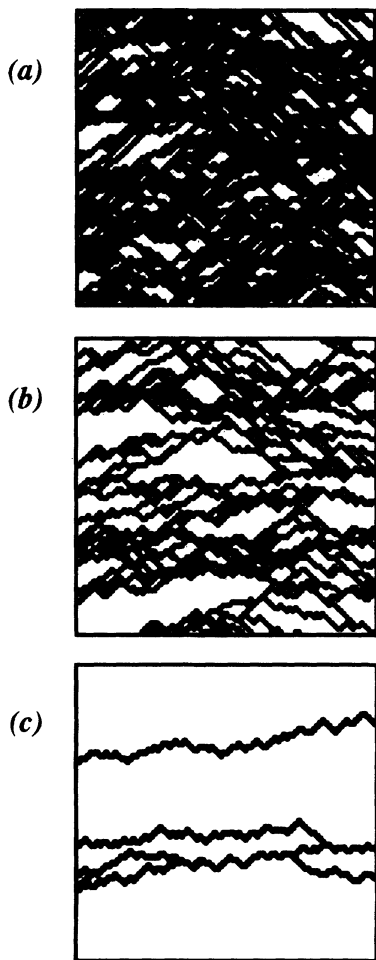


FIG. 7. Exhausted configurations of a single dislocation as calculated from the simple model with  $L = 100$ ,  $\Theta = 6.5$  for stresses of (a)  $\tau = 10.0$ , (b)  $\tau = 12.0$ , and (c)  $\tau = 15.0$ . At low stresses, each exhaustion event produces only small amounts of strain. At stresses near the critical stress, as in panel (b), the events are distributed over many sizes. At stresses above the critical stress [panel (c)], the events are typically very large, sweeping out large areas and lasting for long times. (All three panels represent the same physical size.)

the scale invariance associated with the critical point. Finally, at the critical stress, the characteristic time for the “events” goes to infinity and the scale invariance associated with the critical point is evident in the figure. At this point, the only characteristic time in the system is dictated by the finite size of the dislocation, which, perhaps, corresponds to the time it takes for a superkink to traverse the entire length of the dislocation. Above the critical stress, an infinite mobile dislocation would remain mobile for all times. However, a dislocation of finite length may still be exhausted. This exhaustion process is accomplished not through the dynamics intrinsic to dislocation motion, but rather because the edge of the crystal acts as superkink sinks. This is precisely the situation in Fig. 7(c), where the majority of the “events” are very large.

### B. Scaling properties of the transition

In this subsection, the scaling properties of the transition are explored. The exploration begins with the establishment of scaling behavior for the distribution  $n(a, t) da dt$ , as well as  $\bar{a}(t)$ , and  $v(t, t')$ . The scaling exponents of the transition, defined by the quantities  $\alpha$  and  $\delta$  of Eq. (9), are shown to be near  $\alpha = -\frac{1}{2}$  and  $\delta = -\frac{1}{3}$ . The values of  $\alpha$  and  $\delta$  are then computed as a function of stress from the histograms  $\bar{n}(t) dt$  and  $\bar{n}(a) da$ . The values so obtained are not consistent with the values obtained from  $n(a, t) da dt$ ,  $\bar{a}(t)$ , and  $v(t, t')$  (except near the critical stress). It is argued that this disagreement stems from the presence of the “large events” similar to those of Fig. 7(c) (henceforth referred to as the large events) and hence is a finite-size effect.

The scaling relationship (9) is a very powerful one. Since Eq. (9) must hold for all choices of  $\lambda$ , it must hold for any specific choice. If one chooses  $\lambda = t^{-1/\delta}$ , one can show

$$n(a, t) = t^{1/\delta} f(a/t^{\alpha/\delta}), \quad (27)$$

where  $\alpha$  and  $\delta$  are the scaling exponents appearing in Eq. (9) and  $f(x)$  is a scaling function. Hence plotting  $t^{-1/\delta} n(a, t)$  as a function of  $a/t^{\alpha/\delta}$ , for fixed  $t$ , should result in the scaling function (when at the critical stress). This is explicitly demonstrated for the model in Fig. 8. The system size is  $L = 1000$ ,  $\Theta = 50$ , and  $\tau = 95$ . The critical stress for these conditions is estimated to be  $\tau \approx 95$ . The exponents which produce the best data collapse (where “best” is judged by eye) are  $\alpha = -0.51$  and  $\delta = -0.35$ . These values give  $\Delta = -0.05$ . The magnitudes of the error in the estimates of  $\alpha$  and  $\delta$  obtained in this manner are difficult to assess. Nevertheless, Fig. 8 provides evidence that the  $n(a, t)$  histogram displays scaling behavior over a range of areas and times.

The ratio  $\alpha/\delta$  can also be determined by a direct measurement of the curve of  $\bar{a}(t)$  as a function of  $t$ . Equations (5) and (7) can be used to show that

$$\bar{a}(t) \sim t^{\alpha/\delta}. \quad (28)$$

Figure 9(a) is a plot of  $\bar{a}(t)$  obtained from a system of size  $L = 1000$ , with  $\tau = 95$  and  $\Theta = 50$ . Note that there is a large range of data for which the curve appears straight

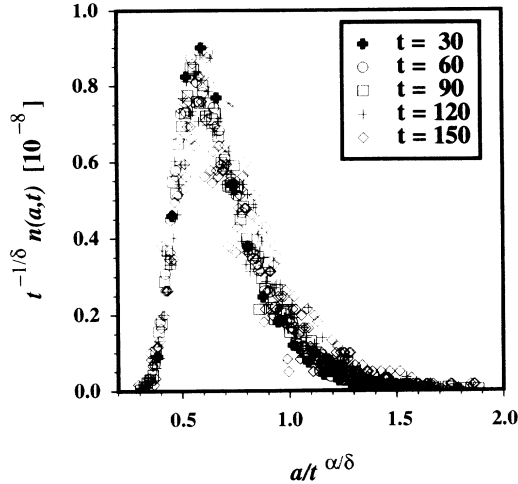


FIG. 8. Plot of  $t^{-1/\delta}n(a,t)$  as a function of  $a/t^{\alpha/\delta}$  with  $\alpha=-0.51$  and  $\delta=-0.35$ . The data were obtained from a simulation with  $L=1000$ ,  $\Theta=50$ , and  $\tau=95$ . The times for each of the curves are indicated in the legend. These values of  $\alpha$  and  $\delta$  give a creep-rate exponent of  $\Delta=-0.05$ , which is well out of the range expected from the TDJ analysis (Ref. 1).

on the log-log plot. The dashed line displays a  $t^{3/2}$  dependence, the dependence suggested by the data collapse in Fig. 8. The long-time behavior shows a linear dependence on time (dotted line). This finite-size effect is discussed further below.

Finally, the ratio  $\alpha/\delta$  can also be determined from the velocity scaling function. Figure 10 is a plot of  $t'^{-1/2}v(t,t')$  as a function of  $t/t'$  for various  $t'$  for data obtained at a stress of  $\tau=90$ , in a system of size  $L=1000$  (the value  $\eta=\frac{1}{2}$  has been used, which is also consistent with the values of  $\alpha$  and  $\delta$  suggested from the scaling plot in Fig. 8). The curves are for times  $t'$  equal to 30, 60, 90,  $\dots$ , 300. The solid line represents the scaling function determined from events with  $t'=30$ . The data collapse on this plot is adequate.

In summary, the data collapse of the scaling functions and the slope of the  $\bar{a}(t)$  curve suggest that the critical exponents (at the transition stress) for this transition are near to  $\alpha=-\frac{1}{2}$ ,  $\delta=-\frac{1}{3}$ ,  $\xi=\frac{3}{2}$ ,  $\beta=\frac{4}{3}$ ,  $\eta=\frac{1}{2}$ , and  $\Delta=0$ . Note that this value of  $\Delta$  is well out of the range assumed by TDJ.<sup>2</sup> Note also that this value of  $\Delta$  and Eq. (18) imply that the time dependence of the primary creep transient is never a simple power law.

In earlier work by the current authors,<sup>10,12</sup> the values of the exponents  $\xi$  and  $\beta$  were determined through analysis of the histograms  $\bar{n}(t)dt$  and  $\bar{n}(a)da$ . The values of the exponents so obtained displayed a stress dependence, which, when convoluted to give the value of  $\Delta$  as a function of stress, agreed with the interpretation of the TDJ results.<sup>1</sup> This analysis is revisited below where it is argued that the apparent stress dependence of the exponents  $\xi$  and  $\beta$ , as measured from  $\bar{n}(t)dt$  and  $\bar{n}(a)da$ , arises from the presence of the large events described above and hence is a finite-size effect.

Figure 11 contains a plot of  $\bar{n}(t)dt$  (with  $dt=1$ ) for four different stresses. (The curves have been offset for clarity.) At lower stresses, the most prominent feature of

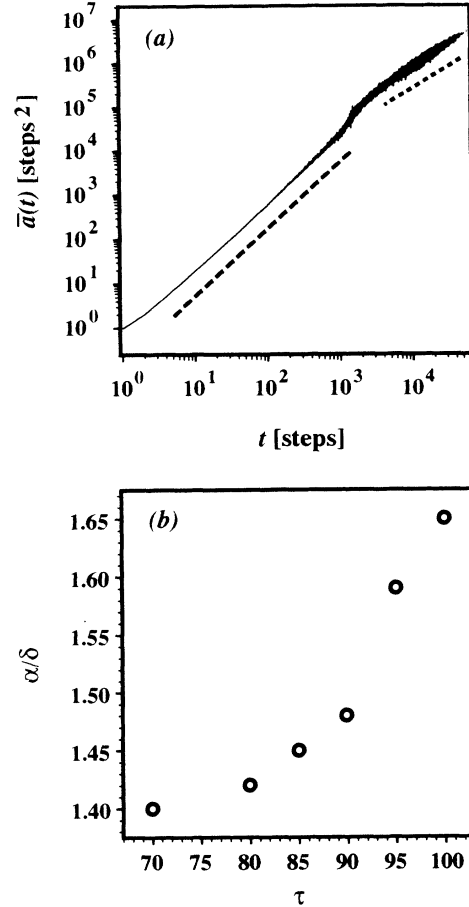


FIG. 9. The solid line in panel (a) is the simulation data for  $\tau=95$ ,  $\Theta=50$ , and  $L=1000$ . The dashed line displays a  $t^{3/2}$  dependence, which tracks the short-time behavior. The dotted line displays linear variation with  $t$ . Panel (b) depicts the stress dependence of the ratio  $\alpha/\delta$  obtained from fits of  $\bar{a}(t)$  to the form of Eq. (28). The data were fit to the range of points with  $10 \leq t \leq 1000$ . Note that the ratio appears nearly constant for  $70 \leq \tau \leq 90$  and then shows a sudden, large increase.

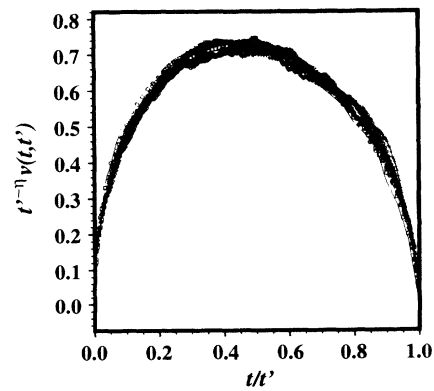


FIG. 10. Plot of  $t'^{-1/2}v(t,t')$  as a function of  $t/t'$  obtained from  $a$  with  $L=1000$ ,  $\Theta=50$ , and  $\tau=90$ , for  $t'=30, 60, 90, \dots, 300$ . The solid line corresponds to  $t'=30$ , and the curves systematically bulge up and to the right with increasing  $t'$ . The value of  $\eta$  was chosen to be  $\frac{1}{2}$ . This value is close to the value of 0.46 suggested from Fig. 8. The data collapse in this plot is adequate.

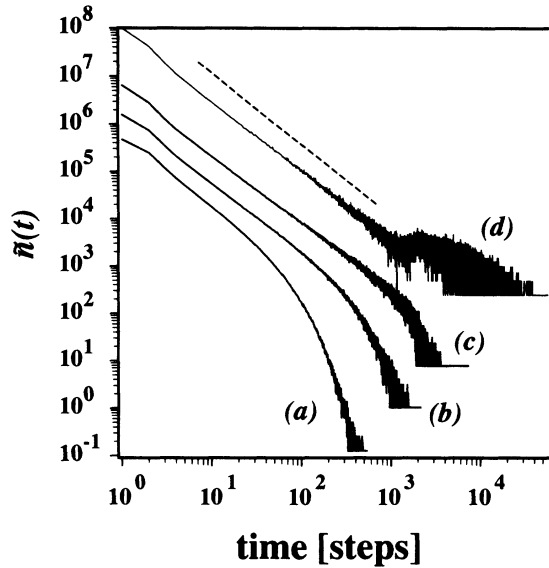


FIG. 11. Plot of  $\bar{n}(t)dt$  (with  $dt=1$ ) as a function of  $t$  as calculated from the simple model for  $\Theta=50$ ,  $L=1000$  at  $\tau=80, 90, 95$ , and  $100$  for curves (a), (b), (c), and (d), respectively. The critical stress for these conditions is estimated to be  $\tau \approx 95$ . The dashed line displays a  $t^{-3/2}$  dependence consistent with the scaling analysis presented in the text. The initial portion of each histogram appears to be near the  $t^{-3/2}$  dependence and then is cut off at longer times, either by a simple exponential dependence [low stresses, curves (a)–(c)] or by the appearance of a peak in the number of large events [high stresses, curve (d)]. This peak is argued to be the result of the finite size of the system.

the curve is the absence of long-time-scale events. At stresses very near the critical stress, e.g., the curves labeled (c) and (d) in the figure, the initial portion of the distribution (excluding the point for  $t=1$  step) is a simple power law. The dashed line displays a  $t^{-3/2}$  dependence—the dependence suggested by scaling analysis presented above. The (d) curve of Fig. 11 also displays a peak at very large times. This peak arises from events similar to those of Fig. 7(c). Simulations on systems with different sizes show that the onset time of the peak scales roughly with system size  $L$ , suggesting that its presence is a finite-size effect. As the stress is further increased, the peak grows, but the onset time appears to remain fixed. The behavior of the  $\bar{n}(a)da$  histograms is very similar to the  $\bar{n}(t)dt$  histograms, including the appearance of an abundance of large events at higher stresses. The small-area portion of the histograms display an  $a^{-4/3}$  dependence, as suggested by the scaling analysis above.

The nature of the proposed transition allows a natural explanation for the origin of the peak. Consider a dislocation being driven below the critical stress. For stresses well below the critical stress, the superkinks responsible for the overall motion of the dislocation are unlikely to traverse its entire length and hence do not feel the presence of the ends of the dislocation. As the stress is increased, the characteristic time for the “events” also increases. Consequently, the superkinks begin to interact

with the free ends of the dislocation more frequently. These events are cut short arbitrarily and appear in the histogram of events,  $n(a,t)da dt$ , at a time and area other than that for which they would appear in an infinite system. Since a superkink moves laterally at the rate of one unit per time step, events that last for a time longer than  $L$  steps are very likely to feel the edge of the dislocation. These events would normally last for much longer than  $L$  steps, but as a consequence of the finite size of the dislocation, they are “folded” into the  $n(a,t)da dt$  histogram at other times. Most often, the time they are folded into is greater than  $L$  steps, but a significant number must also be “folded” into the histogram for times shorter than  $L$  steps. The dynamics governing these large events are not well understood and remains the subject of future research.

The distributions  $\bar{n}(t)dt$  and  $\bar{n}(a)da$  [see Eqs. (3), (4), and (13)] were used to determine  $\xi$ ,  $\beta$ , and  $t_0$ . The numerically obtained histograms were fit to the Ornstein-Zernike form using a standard, generalized least-squares fitting routine, weighting the points of the histogram as if they were governed by Poisson statistics. [The distribution  $\bar{n}(a)da$  was also assumed to have the Ornstein-Zernike form.] The fitted curves were indistinguishable from the numerically obtained histograms.

The values of  $\xi$  and  $\beta$  calculated as a function of the stress parameter  $\tau$  are plotted in Fig. 12, labeled with the subscript 1. These values were obtained by fitting to the range of data  $3 \leq t \leq 1000$ ,  $10 \leq a \leq 8000$  for a dislocation of size  $L=1000$  and  $\Theta=50$ . The most notable feature of this plot is that the exponents  $\xi$  and  $\beta$  are apparently stress dependent. A parameter-dependent critical exponent is *not* expected from the analogy with equilibrium critical phenomena, and so this result is somewhat

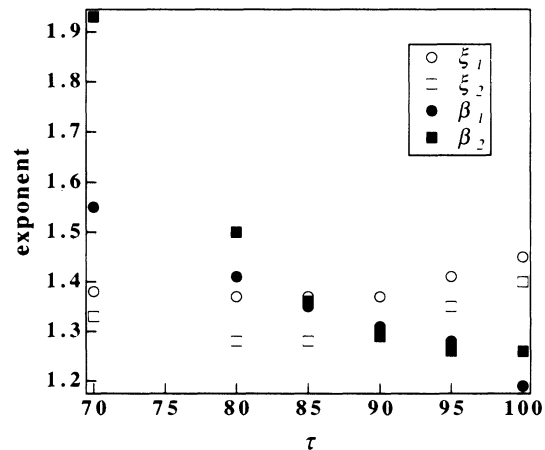


FIG. 12. Plot of the exponents  $\beta$  and  $\xi$  as a function of the applied stress calculated for a system with  $L=1000$  and  $\Theta=50$ . The exponents labeled with the subscript 1 arise from fits to the simulation results for the range  $3 \leq t \leq 1000$  and  $10 \leq a \leq 8000$ . The exponents with the subscript 2 are those calculated by fitting the data from the simulations over the range  $20 \leq t \leq 500$  and  $50 \leq a \leq 3000$ . Note that in both cases the exponents depend on the applied stress. Also, note that the results from the two fits are not coincident.

surprising. Three possible explanations for this behavior are that (1) the critical exponents truly do vary as a function of stress, (2) the variation is an artifact of the fitting procedure, in particular, the choice of the Ornstein-Zernike form for  $\bar{n}(t)$ , or (3) the finite size of the system is playing an important role. Evidence in favor of explanations (2) and (3) is presented in Fig. 12, which also plots the values of  $\xi$  and  $\beta$  obtained by fitting the same functional form to a smaller range of the numerical data:  $20 \leq t \leq 500$  and  $50 \leq a \leq 3000$ , labeled by the index 2. Note that the two sets of data are not coincident and can differ by as much as 25%. The implication is that Eq. (13) does not provide an accurate description of the histograms.

Because both  $\xi$  and  $\beta$  appear to depend on the applied stress  $\tau$ , the value of  $\Delta$  calculated from these exponents [using Eqs. (10)–(12)] is also stress dependent, as has been noted in the previous work.<sup>10,12</sup> At low stresses, the  $\Delta$  is near 1, predicting logarithmic creep. At higher stresses, the creep-rate exponent decreases, implying a power-law time dependence for the primary-creep transient. Finally, the creep-rate exponent approaches  $\Delta(\tau) \sim 0$  at the transition stress, which is consistent with the values obtained through the data-collapse plot in Fig. 8.

The origin of the discrepancy between the critical exponents determined from the data-collapse plot (Fig. 8) and those determined by  $\bar{n}(t)dt$  and  $\bar{n}(a)da$  is now discussed. Insight into the discrepancy can be obtained when one plots the value of  $\alpha/\delta$  obtained from the measurements of  $\bar{a}(t)$  as a function of the stress parameter  $\tau$ . Figure 9(b) contains this plot. Note that  $\alpha/\delta$  slowly varies over the range of stresses  $70 \leq \tau \leq 90$ , but then shows a rapid increase. The data were fit to the range of points with  $10 \leq t \leq 1000$ . The marked rise in the value of  $\alpha/\delta$  near  $\tau=95$  stems from the presence of the large-scale events of Fig. 7(c). Note also that the simulation data [Fig. 9(a)] shows two regimes. A short-time regime, whose slope is near to that expected from a  $t^{3/2}$  dependence (indicated by the dashed line in the figure), and a long-time regime, with a slope corresponding to a linear dependence on  $t$  (i.e., a constant velocity for the dislocations, indicated by a dotted line). Figure 9 implies that the critical exponents  $\alpha$  and  $\delta$  are dependent weakly, at most, on stress for times  $t \leq 1000$  steps. Near the critical stress, however, the large events skew the results of the fits.

The values  $\xi = \frac{3}{2}$  and  $\beta = \frac{4}{3}$  deduced from the data collapse of the scaling functions and the  $\bar{a}(t)$  curves are in reasonable agreement with the initial dependence (small  $t$  and  $a$ ) of the  $\bar{n}(t)dt$  and  $\bar{n}(a)da$  plots. *The internal consistency of the data suggests that the estimates of the scaling exponents based on the data collapse of the  $n(a, t)da dt$  plots are the most accurate.*

In summary, the dislocation exhaustion events can have one of two behaviors: (1) a small event which displays scaling behavior and (2) a large event. The data collapse plots, which are composed of events from shorter times, are less susceptible to the presence of the large events (which tend to appear at larger times). In contrast, the fits of  $\bar{n}(t)dt$  and  $\bar{n}(a)da$  to the Ornstein-Zernike form are influenced by the presence of large

events. These large events do not display the same scaling behavior as the small events and, hence, are not well described by the Ornstein-Zernike form. The presence of the large events, whose number increases with applied stress  $\tau$ , explains the apparent stress dependence of  $\Delta$  reported in Refs. 10 and 11.

Given this understanding (which was not appreciated by the current authors in their prior work), it is not obviously appropriate to associate the apparent stress dependence of  $\Delta$  with that deduced from the TDJ data.<sup>1</sup> The agreement between the experiments and simulations as reported in Refs. 10 and 12 is, therefore, fortuitous. It is not, however, correct to conclude that the model studied here is not a good description of the physics of the transition. Perhaps the agreement between the analysis of Refs. 10 and 12 and TDJ's interpretation of their data stems from applying the same approximation to both the results of the experiments and simulations. In this view, it is the interpretation of the model results (and earlier experiments) that is flawed, not the model itself. A comparison presented below shows that the model is consistent with the TDJ data, although further experiments are needed.

Large events are also expected in experiments. However, the scaling theory is expected to apply for applied stresses in which the contribution to the strain from the large events is "small," i.e., for times  $t < t_0$  and at stresses for which  $t_0$  is less than the time it takes for a superkink to traverse the width of the crystal. Consequently, in the next section, the predictions of the Ornstein-Zernike-based description [Eq. (18)], while fixing the exponents to the values  $\alpha = -\frac{1}{2}$ ,  $\delta = -\frac{1}{3}$ ,  $\xi = \frac{3}{2}$ ,  $\eta = \frac{1}{2}$ , and  $\Delta = 0$ , are investigated. A more complete theory (i.e., applicable to a broader range of times), including the effects of the large events, has not been developed.

## V. IMPLICATIONS FOR EXPERIMENTS

The exponents measured from the simple model are most consistent with the values  $\alpha = -\frac{1}{2}$  and  $\delta = -\frac{1}{3}$ . With these values the creep rate, Eq. (18) becomes

$$\frac{d\gamma(t)}{dt} = \frac{\bar{n}_t b}{V} \sum_{m=0}^{\infty} g_m \int_1^{\infty} \frac{dx \exp(-xt/t_0)}{x^{m+1}}, \quad (29)$$

where  $b$  is the magnitude of the Burgers vector,  $\bar{n}_t$  is the normalization constant for the distribution of exhaustion times, and  $V$  is the crystal volume. Thus the conjecture contained in Eq. (13) plays a crucial role in determining the creep behavior. The integral is the well-studied exponential integral

$$E_n(t/t_0) \equiv \int_1^{\infty} \frac{dx \exp(-xt/t_0)}{x^n}. \quad (30)$$

Equation (29) can be integrated from some initial time  $t_{\text{init}}$  to give the following expression for the creep curve:

$$\begin{aligned} \gamma(t) = & \gamma(t_{\text{init}}) \\ & + \frac{\bar{n}_t b}{V} t_0 \sum_{m=0}^{\infty} g_m [E_{m+2}(t_{\text{init}}/t_0) - E_{m+2}(t/t_0)]. \end{aligned} \quad (31)$$

Note that expression (31) does not apply for  $t_{\text{init}}=0$ , because  $\bar{n}(t)$  is no longer of the form given by Eq. (13).

Expression (31) holds the promise of allowing the direct measurement of the areal-velocity scaling function  $g(x)$ . One can fit the experimentally obtained primary-creep transient to the form of Eq. (31). This fitting procedure results in a polynomial approximation to  $g(x)$ . The areal-velocity scaling function has a physically important interpretation. It describes the average velocity of a dislocation destined to be exhausted at some time. Since this velocity is determined by the superkink distribution, the form of this curve gives direct insight into the nature of the fluctuations in the superkink population. In the model studied here, the dislocation motion is initiated at some superkink structure, the velocity increases for some time as the superkinks grow in size and multiply, and finally, the velocity decreases through superkink annihilation. This behavior is evident from the form of the scaling function in Fig. 10. The fluctuations display scale invariance; the only time scale for the fluctuation is set by the total length of time for which the dislocation is mobile. Thus simple measurement of the primary-creep transient should result in a direct measurement of the dynamic properties of the superkink population.

As a test of this analytical technique, the creep curve resulting directly from the simulations was fit to the form of Eq. (31), retaining all terms in the sum with  $m \leq 4$  and fixing the coefficients  $g_m$  to have the values measured from the data collapse plots for the areal velocity scaling function. The parameters  $\gamma(t_{\text{init}})$ ,  $\bar{n}_t$ , and  $t_0$  were allowed to vary. Two fitted creep curves are compared with the numerically calculated creep curve in Fig. 13. The data were collected from a simulation with  $L = 1000$ ,  $\Theta = 50$ , and  $\tau = 90$ . The dashed line is fit to the entire range of data; the dotted line is fit the range  $10 \leq t \leq 300$ .

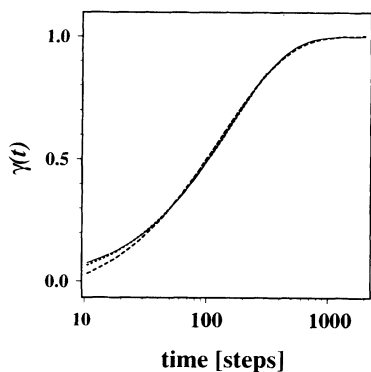


FIG. 13. Comparison of expression (31) with the creep curve resulting directly from the simulations. The creep curve was obtained for a stress of  $\tau=90$ . The areal-velocity scaling function was measured directly and fit to a polynomial retaining terms  $x^m$  with  $m \leq 4$ . This polynomial approximation was used to fit the simulation results to expression (31) allowing only  $\gamma(t_{\text{init}})$ ,  $\bar{n}_t$ , and  $t_0$  to vary. The dashed line is the fit to the entire range of data shown and gives  $t_0=320$  steps. Expression (31) is expected to hold only for times less than  $t_0$ . The dotted line in the figure, nearly indistinguishable from the simulation results, is the curve fit to the range of data:  $10 \leq t \leq 300$  steps.

The dashed fitted curve and the simulation are similar, although the agreement is not perfect. The differences between the fitted curve and the simulation results arise primarily from the fact that expression (14) for the areal-velocity scaling function holds only for  $t \ll t_0$  ( $t_0=320$  steps from the fit). The dotted line is indistinguishable (except from 10 to 20 steps) from the simulation result and results in  $t_0=410$  steps. Thus expression (31) provides an *excellent* description of the appropriate range of data, as dictated by  $t_0$ .

As a final note, Fig. 14 displays the result of fitting the TDJ data to the form of Eq. (31). Note that these data are taken from the TDJ “ $t^{1/3}$  regime.” The data reported in this regime are believed to be obtained in the correct range of applied stresses for expression (31) to be applicable. The limited number of available data points, coupled with uncertainties introduced by the polycrystallinity of the samples (more than one slip system may be operative), suggests that this fitting procedure is not a stringent test of the theory. Figure 14 is presented only for illustrative purposes. It is clear that Eq. (31) provides an adequate description of the data. Clearly, experiments on single-crystal specimens oriented for single-system slip are necessary.

The properties of the characteristic time  $t_0$  appearing in Eq. (31) are also of possible experimental interest. In general,  $t_0$  will be stress dependent. As the stress increases, so will  $t_0$ . In an infinite system,  $t_0 \rightarrow \infty$  at the critical stress, and there is no characteristic exhaustion time. In a finite system, however, one can never eliminate all time scales. At the critical point for the small events, the only remaining time scale for these events is the typical time it takes for a superkink to traverse the entire dislocation. Thus, as the stress increases,  $t_0$  should increase until it reaches the traversal time. Further increases in stress should only *decrease*  $t_0$ , assuming that the superkinks move more rapidly under higher applied stresses.

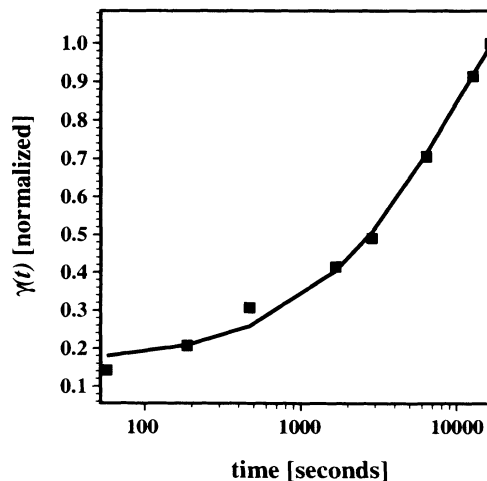


FIG. 14. Test of the fitting procedure on the TDJ data for 363 MPa and a temperature of 399°C. Only the  $m=0$  term of Eq. (31) is included in the fit. The paucity of data points and the uncertainties introduced by the polycrystallinity of the sample make a quantitative test of Eq. (31) difficult.

## VI. CONCLUSIONS

It has been argued that the dislocations in the  $L_{12}$  intermetallic alloys displaying the yield strength anomaly undergo a stress-driven pinning-depinning transition. The transition is from a "phase" in which all dislocation motion is ultimately exhausted to a "phase" in which a mobile dislocation remains mobile for all time for a dislocation of infinite length.

The scaling properties of the transition were studied using a model of dislocation motion. In particular, it was argued that there are two types of events: large and small. The small events were shown to display scaling behavior, whereas the large events, which result from the finite size of the system, displayed different behavior. The critical exponents of the transition were obtained from the properties of the small events. These critical exponents differ from earlier estimates of their values.<sup>10,12</sup> The differences were attributed to the presence of finite-size effects. It is suggested that the agreement between experiment and the theory reported in Refs. 10 and 12 stems from applying the assumption of a power-law time dependence to both the experimental and numerically calculated transients.

The nature of the primary-creep transients predicted

by the model were explored by assuming the critical exponents of the transition are those deduced from the small events. It was argued that for a range of stresses below the critical stress, Eq. (31) provides a good description of the creep transient. Comparison of expression (31) to the TDJ data supports this argument, although further experiments designed explicitly for testing the theory are warranted.

Finally, it is noted that within the model presented here, the primary-creep transient can be used to directly measure the properties of the dislocation areal-velocity scaling function. These measurements can provide important experimental information concerning the dynamical properties of the dislocations. These properties can then be used to refine the theories of dislocation motion.

## ACKNOWLEDGMENTS

The authors gratefully acknowledge conversations with M. S. Daw, S. M. Foiles, W. G. Wolfer, G. S. Bales, G. Saada, and M. Marder. Support for this research was provided by the U.S. Department of Energy, Office of Basic Energy Sciences, Division of Materials Sciences under Contract No. DE-AC04-94AL85000.

<sup>1</sup>P. H. Thornton, R. G. Davies, and T. L. Johnston, *Metall. Trans.* **1**, 207 (1970).

<sup>2</sup>J. Stoiber, J. Bonneville, and J. L. Martin, in *Proceedings of the International Conference on the Strength of Metals and Alloys (ICSMA 8)*, edited by P. O. Kettunen, T. K. Lepistö, and M. E. Lehtonen (Pergamon, New York, 1988), Vol. 1, p. 457.

<sup>3</sup>P. Veyssi re, *Rev. Phys. Appl.* **23**, 673 (1988).

<sup>4</sup>M. S. Duesbery, in *Dislocations in Solids*, edited by F. R. Nabarro (Elsevier, Amsterdam, 1989), p. 67.

<sup>5</sup>B. H. Kear and H. G. F. Wilsdorf, *Trans. Metall. Soc. AIME* **224**, 382 (1962).

<sup>6</sup>P. A. Flinn, *Trans. Metall. Soc. AIME* **218**, 145 (1960).

<sup>7</sup>M. H. Yoo, *Scr. Metall.* **20**, 915 (1986).

<sup>8</sup>V. Paidar, D. P. Pope, and V. Vitek, *Acta Metall.* **32**, 435 (1984).

<sup>9</sup>M. J. Mills and D. C. Chrzan, *Acta Metall. Mater.* **40**, 3051 (1992).

<sup>10</sup>D. C. Chrzan and M. J. Mills, *Mater. Sci. Eng. A* **164**, 82 (1993).

<sup>11</sup>Y. Q. Sun and P. M. Hazzledine, *Philos. Mag. A* **58**, 603 (1988); A. Korner, *Philos. Mag. Lett.* **58**, 507 (1988); P. Veyssi re, in *High Temperature Ordered Intermetallic Alloys III*, edited by C. T. Liu, A. I. Taub, N. S. Stoloff, and C. C. Koch, MRS Symposia Proceedings No. 133 (Materials Research Society, Pittsburgh, 1989), p. 175; M. J. Mills, N. Baluc, and H. P. Karnthaler, *ibid.*, p. 203.

<sup>12</sup>D. C. Chrzan and M. J. Mills, *Phys. Rev. Lett.* **69**, 2795 (1992).

<sup>13</sup>D. S. Fisher, *Phys. Rev. B* **31**, 1396 (1985).

<sup>14</sup>H. E. Stanley, *Introduction to Phase Transitions and Critical Phenomena* (Oxford University Press, New York, 1971).

<sup>15</sup>S.-K. Ma, *Modern Theory of Critical Phenomena* (Benjamin/Cummings, Reading, MA, 1978), p. 33.

<sup>16</sup>See J. Krug and H. Spohn, in *Solids far from Equilibrium*, edited by C. Godr che (Cambridge University Press, Cambridge, England, 1992), p. 479, and references therein.

<sup>17</sup>E. J. Ding and Y. N. Lu, *Phys. Rev. Lett.* **70**, 3627 (1993).

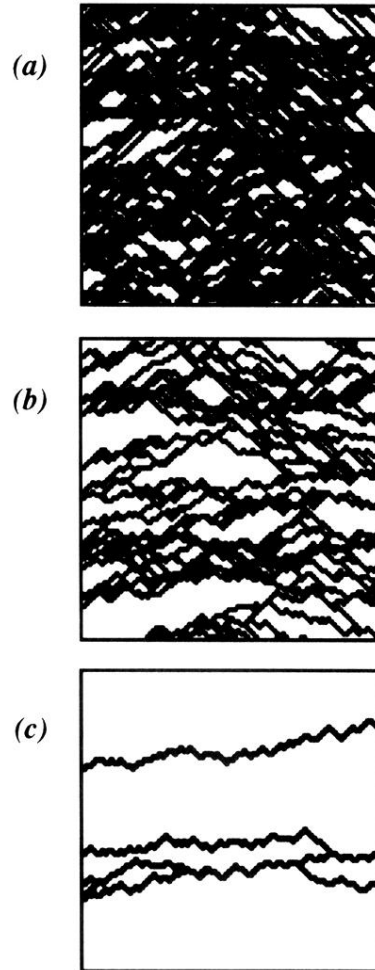


FIG. 7. Exhausted configurations of a single dislocation as calculated from the simple model with  $L=100$ ,  $\Theta=6.5$  for stresses of (a)  $\tau=10.0$ , (b)  $\tau=12.0$ , and (c)  $\tau=15.0$ . At low stresses, each exhaustion event produces only small amounts of strain. At stresses near the critical stress, as in panel (b), the events are distributed over many sizes. At stresses above the critical stress [panel (c)], the events are typically very large, sweeping out large areas and lasting for long times. (All three panels represent the same physical size.)